

Predicting the Mechanical Properties of Fibrin Using Neural Networks Trained on Discrete Fiber Network Data

Yue Leng¹, Sarah Calve^{1,2} and Adrian B Tepole^{1,3}

¹*Weldon School of Biomedical Engineering, Purdue University, West Lafayette, IN, USA*

²*Department of Mechanical Engineering, Colorado University, Boulder, CO, USA*

³*School of Mechanical Engineering, Purdue University, West Lafayette, IN, USA*

Abstract

Fibrin is a structural protein key for processes such as wound healing and thrombus formation. At the macroscale, fibrin forms a gel and the overall mechanical response is dictated by the mechanics of a microscale fiber network. Hence, accurate description of fibrin gels can be achieved using representative volume elements (RVE) that explicitly model the discrete fiber networks of the microscale. These RVE models, however, cannot be efficiently used to model the macroscale due to the challenges and computational demands of coupling the micro- and macroscale models. Here, we propose the use of an artificial, fully connected neural network (FCNN) to efficiently capture the behavior of the RVE models. The FCNN was trained on 1100 discrete fiber networks subjected to 121 biaxial deformations. The stress data from the RVE, together with the total energy on the fibers and the condition of incompressibility of the surrounding matrix, were used to determine the derivatives of an unknown strain energy function with respect to the deformation invariants. During training, the loss function was modified to ensure convexity of the strain energy function and symmetry of its Hessian. An invariant representation is compatible with standard finite element codes. Thus, a general FCNN model was coded into a user material subroutine (UMAT) in the commercial software Abaqus. The UMAT implementation takes in the structure and parameters of an arbitrary FCNN as material parameters from the input file. The inputs to the FCNN include the first two isochoric invariants of the deformation, and the FCNN outputs are the derivatives of the strain energy with respect to the isochoric invariants. Second derivatives of the strain energy function are automatically calculated inside the UMAT through back-propagation. In this work, the FCNN trained on the discrete fiber network data was used in finite element simulations of fibrin gels using our UMAT. We anticipate that this work will enable further integration of machine learning tools with standard computational mechanics tools such as finite element analysis. It will also improve computational modeling of biological materials characterized by a multiscale structure.

Keywords: Machine Learning, Nonlinear finite elements, Constitutive modeling, Abaqus User Subroutine UMAT, Multiscale modeling

Introduction

It is well known that the biomechanical macroscopic behavior of both native and engineered tissues is largely determined by the properties of the underlying microstructural components [1]. Therefore, to allow for a better design of engineered tissues and to increase our fundamental understanding of the mechanical behavior of soft tissue, it is necessary to investigate this multiscale coupling. Fibrin is an important extracellular matrix (ECM) component in the body, providing structural integrity to various tissues [2, 3]. It plays a critical role in wound healing and thrombus fate [4, 5]. In addition, it is also a common scaffold material used in tissue engineering [6]. The fibrin network structure can be described by variables such as the fiber diameter and length, the number of branch points, and the volume fraction [7].

Due to the inherent multiscale nature of fibrin gels, with the macroscopic dimension described at the centimeter length scale and the underlying fibrin network defined at the micrometer length scale, our understanding of the macroscale mechanics needs to be informed by the microscale mechanical behavior of the fibrin network. To enable

the multiscale description, models of discrete fiber networks (DFN) in a representative volume element (RVE) have often been proposed [8, 9]. These micromechanical models, based on volume average theory, assumed that the stress and strains at the macroscopic scale are volume averages of the corresponding microscale fields in the RVE, and thus provide the linkage between the fiber-level mechanics and the tissue-level behaviors [7, 10, 11]. DFN models are able to predict the mechanical behavior of three-dimensional fibrin networks. The volume-averaging homogenization that satisfies the Hill-Mandel condition can then be used as a constitutive model at the macroscale, where the standard balance of linear momentum within continuum mechanics can be solved to determine the mechanical response [12, 13]. Moreover, at the macroscale, hyperelasticity is a common assumption that is used to describe soft tissue mechanics [14, 15]. Numerically, the macroscale response can be efficiently modeled within a nonlinear finite element framework. The standard coupling between the macroscale and microscale descriptions, however, entails the simulation of individual RVEs associated with each of the integration points of the finite element simulation. This strategy of nesting DFN models within the finite element framework for large-scale heterogeneous structures is computationally prohibitive. Not surprisingly, their use has been limited [16, 17].

A myriad of strategies for model order reduction have been implemented to predict the mechanical properties of multiscale materials that balance computational cost and accuracy [18, 19, 20, 21, 22]. In particular, machine learning (ML) methods have been extended to various problems of mechanics modeling and multiscale simulations, e.g., modeling macroscopic material behavior by stress-strain curves obtained from micromechanical simulations [17]; approximating the surface response and deriving the macroscopic stress and tangent tensor components [23]; capturing the multiscale hydro-mechanical coupling effect of porous media with pores of varying sizes [24], and predicting the stress-strain behavior of binary composites [25].

The neural network method is one example of a ML technique that is capable of extracting meaningful relationships from data given a sufficient amount of training data. This method is efficient in automatically discovering and capturing the underlying complex high-dimensional mapping from the feature vector input to the desired output without the need of manually deriving specific functional forms [26, 27].

In this paper, we propose a novel multiscale modeling approach that employs fully connected neural networks (FCNN) to describe the homogenized response of simulations of DFNs. The FCNN is able to predict the mechanical response of various microstructures under different loads. In this way, the trained FCNN represents a new macroscopic constitutive relation. To develop the FCNN metamodel, we first generated training data by creating a large number of DFN microstructures and subjecting the RVEs to various biaxial loading conditions. Derivatives of the strain energy with respect to the strain invariants were obtained by creating a Gaussian process (GP) surrogate for the strain energy further constrained on the observed stress data. Using the values of the derivatives of the strain energy as the data, we trained a FCNN model to predict the mechanical properties (e.g., stress and elasticity tensor) of a composite based on its microstructure and the value of the strain invariants. Notably, the convexity of the strain energy, which is essential to ensure the model is physically meaningful and numerically stable when the FCNN is used in finite element simulations, was considered in the training process by specifically defining the loss function to enforce these constraints. Following training, we tested the FCNN by comparing the prediction against the ground truth DFN model on a validation set. Finally, we implemented the FCNN in a general User Material Subroutine (UMAT) in the popular finite element package Abaqus.

Our work demonstrates that neural networks can be trained by micromechanical simulations, which capture ECM network behavior accurately. The main features of our model are the invariant formulation of the FCNN which satisfies stress objectivity *a priori*, the imposition of a convexity constraint on the strain energy function for numerical stability, the effective inference of the nonlinear map, and the implementation of arbitrary FCNN as a UMAT subroutine in Abaqus. We anticipate that this work will enable the widespread use of ML-driven multiscale simulations by reducing the computational cost without compromising accuracy.

Materials and Methods

Discrete fiber network models

In the DFN model, multiple fibers were linked to each other through cross-links, and they were allowed to stretch, compress, or rotate at these points. Bending forces were not considered during fiber deformation. The procedure for the generation of the networks was in a similar manner to previous efforts [7, 28]. Namely, we seeded the three-dimensional RVE with random uniformly distributed nucleation points. Each point gave rise to two segments, which

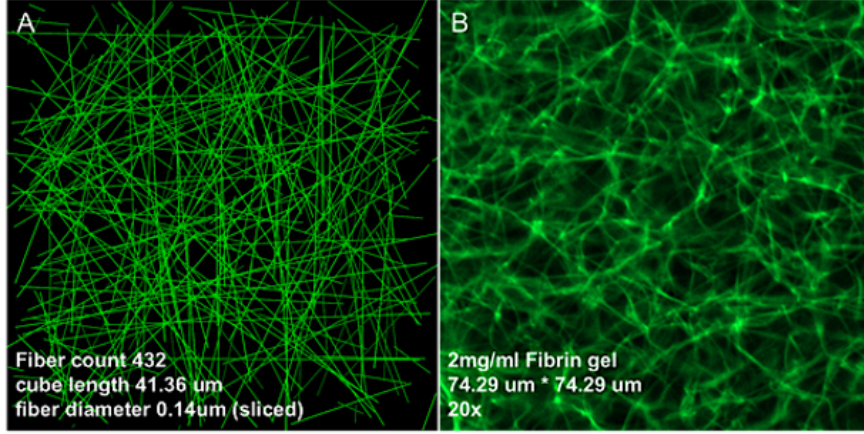


Figure 1: A microscale network model (A), was used to simulate the fibrin networks (B).

grew oppositely along a randomly chosen direction sampled from a uniform distribution on the unit sphere. At each step of fiber growth, every segment was checked to decide if it had exceeded the boundaries of the cube or had collided with another segment. At the point of the identified intersection or collision, a node was introduced, and the segment stopped growing. When the growth of all the segments stopped, the algorithm of fibrillar network generation terminated. A sample image of a DFN is depicted in Figure 1A, alongside a confocal image of a 2mg/ml fibrin gel in Figure 1B.

Applying forces or deformations to the boundaries of the RVE leads to the deformation of the fibers inside of the network. Individual fibers were considered as hyperelastic and the state of mechanical equilibrium was determined by finding the minimum of the total energy in the fibers. The energy in a fiber i in the network is

$$\Psi_f^{(i)} = \frac{k_f}{2} \left((\lambda_f^{(i)})^2 - 1 \right), \quad (1)$$

where the stretch of the fiber i is given by

$$\lambda_f^{(i)} = \frac{\|\mathbf{x}_1^{(i)} - \mathbf{x}_0^{(i)}\|}{\|\mathbf{X}_1^{(i)} - \mathbf{X}_0^{(i)}\|}, \quad (2)$$

$\mathbf{X}_0^{(i)}, \mathbf{X}_1^{(i)}$ denote the reference coordinates of the nodes making up the fiber, and $\mathbf{x}_0^{(i)}, \mathbf{x}_1^{(i)}$ the location of the nodes after deformation. The material parameter k_f is the stiffness of the fiber. The mechanical equilibrium is obtained by searching for the deformed nodal coordinates of all the fibers such that the total energy $\sum_i \Psi_f^{(i)}$ is minimized. The boundary conditions are imposed displacements on all nodes at the boundary of the RVE. The homogenized stress on the RVE is calculated based on the averaging [7],

$$\sigma^M = \langle \sigma^\mu \rangle = \frac{1}{V} \int_{RVE} \sigma^\mu. \quad (3)$$

σ^M denotes the macroscale stress, which is the average of the microscale stress field σ^μ over the RVE volume V . For the DFN, the stress can be written in indicial notation as

$$\sigma_{ij}^M = \frac{1}{V} \sum x_i^b R_j^b \quad (4)$$

where the sum is over the deformed coordinates of the boundary nodes, \mathbf{x}^b , and the corresponding reaction forces \mathbf{R}^b .

To generate enough training data for the FCNN, a total of 1100 networks were generated. To explore the different network geometries, two quantities of interest were identified as the best descriptors for microstructure: the volume

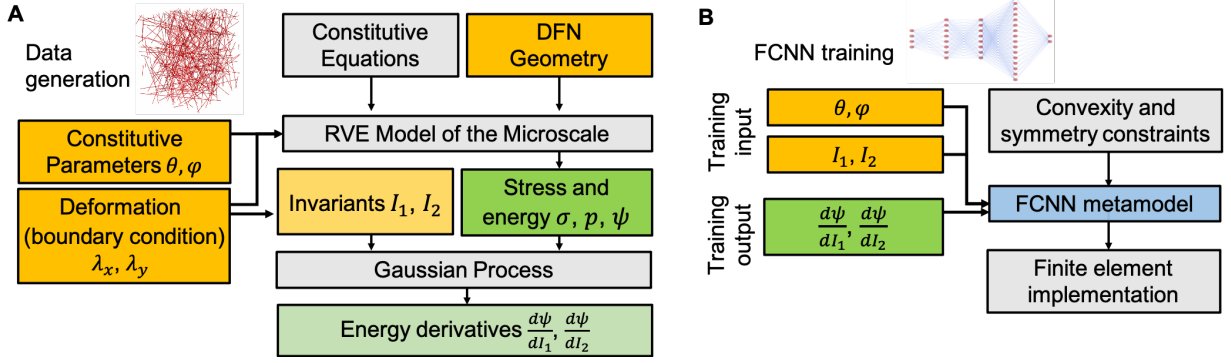


Figure 2: Framework for training a ML-based microscale model. Input data was generated by sampling from microstructure θ , φ , and deformation parameters λ_x , λ_y , which were post-processed to obtain the invariants I_1 , I_2 . Multiple random geometries were sampled for a given microstructure and deformation. The RVE model was evaluated to generate output stress and strain energy, which were post-processed through Gaussian process regression and optimization to obtain energy derivative outputs (A). A fully connected neural network (FCNN) was trained on a training subset of the data, and tested on a different subset of data. FCCN training was further constrained to satisfy convexity and symmetry, requirements for a stable finite element implementation (B).

fraction θ , and the fiber diameter φ . The range of the model parameters was obtained to span similar networks to those reported in the literature [7, 29]. Namely, the diameter φ was in the range of [20 – 500] nm, and the volume fraction was in the range $\theta \in [0.05, 1.0]\%$.

Following the generation of the 1100 different RVE microstructures, data of stress and energy for each of these RVEs under various deformation regimes were generated. Analogous to mechanical tests performed to characterize soft material mechanics, the RVEs were subjected to biaxial deformation under plane stress. Eleven stretches in the x axis were selected $\lambda_x = [1.00, 1.025, 1.05, 1.075, 1.10, 1.125, 1.15, 1.175, 1.2, 1.225, 1.25]$. Similarly for the y axis, we used $\lambda_y = [1.00, 1.025, 1.05, 1.075, 1.10, 1.125, 1.15, 1.175, 1.2, 1.225, 1.25]$. The deformations applied to the RVE were all the possible combinations of λ_x and λ_y from the values above, i.e. a total of 121 simulations per RVE were run for the training of the ML metamodel. The transverse stretch was calculated to maintain incompressibility. While not used for training of the ML metamodel, uniaxial simulations were also explored to compare against previous reports in the literature.

Hyperelastic material behavior at the macroscale

In the multiscale formulation, the average stress of the homogenized RVE, $\sigma^M = \langle \sigma^\mu \rangle$, is a function of the average deformation gradient $\mathbf{F}^M = \langle \mathbf{F}^\mu \rangle$. In practice, the average deformation gradient known from the macroscale, \mathbf{F}^M , is imposed as a boundary condition to the RVE. Mechanical equilibrium of the RVE then yields the microscale field σ^μ , which is averaged to compute the corresponding stress σ^M . In this way, the relationship $\sigma^M(\mathbf{F}^M)$ is implied although not available explicitly, and it needs instead the evaluation of the RVE model. Under the additional assumption that the macroscopic material behavior is that of a nearly incompressible hyperelastic material [30, 31], we propose the existence of a strain energy function Ψ

$$\Psi = \Psi_{\text{iso}}(\bar{I}_1, \bar{I}_2) + \Psi_{\text{vol}}(J) \quad (5)$$

with the standard definition of the isochoric strain invariants and the volume change

$$\bar{I}_1 = \text{tr}(\bar{\mathbf{b}}) = \bar{\mathbf{b}} : \mathbf{I}, \quad \bar{I}_2 = \frac{1}{2} \left((\text{tr}(\bar{\mathbf{b}}))^2 - \text{tr}(\bar{\mathbf{b}}^2) \right), \quad J = \det(\mathbf{F}^M). \quad (6)$$

Furthermore, the invariants in eq. 6 require the definition of the isochoric left Cauchy-Green deformation tensor,

$$\bar{\mathbf{b}} = J^{-2/3} \mathbf{b} = J^{-2/3} \mathbf{F}^M (\mathbf{F}^M)^T. \quad (7)$$

Note that the deformation metrics defined in eqs. (6) and (7) are with respect to the macroscale deformation. The strain energy function in (5) is not analytically available, but its existence implies that

$$\sigma^M = 2\bar{\mathbf{b}} \frac{\partial \Psi}{\partial \bar{\mathbf{b}}} = \mathbb{P} : \bar{\sigma} + p\mathbf{I} = \bar{\sigma} - \frac{1}{3}\text{tr}(\bar{\sigma}) + p\mathbf{I}, \quad (8)$$

where we have introduced the fictitious stress and the pressure,

$$\bar{\sigma} = 2\bar{\mathbf{b}} \frac{\partial \Psi_{\text{iso}}}{\partial \bar{\mathbf{b}}}, \quad p = \frac{\partial \Psi_{\text{vol}}}{\partial J}. \quad (9)$$

Finally, to compute the fictitious stress in (9), the derivatives $\Psi_1(\bar{I}_1, \bar{I}_2) = \partial \Psi_{\text{iso}} / \partial \bar{I}_1$ and $\Psi_2(\bar{I}_1, \bar{I}_2) = \partial \Psi_{\text{iso}} / \partial \bar{I}_2$ are needed, and, like the strain energy, these derivatives are also functions of the isochoric invariants. Thus, knowledge of the functions $\Psi_1, \Psi_2, \Psi_{\text{vol}}$ are enough to compute the stress at the macroscopic level σ^M . It is remarked again that these functions are not analytically available. The approach presented here relies on computing the stress and energy of the fibers from solving the RVE model upon application of the macroscale deformation \mathbf{F}^M as a boundary condition. Then, a FCNN can be trained to represent the functions Ψ_1, Ψ_2 that best represent the stress data from the RVE simulations.

Strain energy and its derivatives using Gaussian processes and optimization

A Gaussian process (GP) is a stochastic process whose value at any collection of data points can be described with a multivariate normal distribution [32]. Consider a data set comprised of input-output pairs $\mathcal{D} = \{\mathbf{x} = (I_1, I_2), \Psi_f\}$, where I_1 and I_2 are the invariants of the corresponding deformation \mathbf{F}^M applied to the RVE, and $\Psi_f = \sum \Psi_f^{(i)}$ is the total strain energy accumulated in the fibers of the RVE. The data set \mathcal{D} consists of the vector of inputs and outputs from all the training simulations. We used a GP to describe these data. The prior of the GP is fully determined by a mean function and a covariance function. A zero-mean prior was considered. For the covariance function we used a radial basis function (RBF) kernel [33]. This kernel is also commonly referred to as the squared exponential kernel. The implementation of the GP in the Python package *GPpy* was used [34]. The hyperparameters of this kernel are the length scale and signal strength, which were optimized to maximize the likelihood of the observed data pairs. After fitting, the posterior GP is denoted $\Psi_f^*(I_1, I_2)$, and it can be used to make predictions at points $\mathbf{x}^* = (I_1^*, I_2^*)$ that were not part of the training data. The predicted strain energy Ψ_f^* at a new point \mathbf{x}^* is a GP with mean function

$$\mu_f = \mathbf{k}(\mathbf{x}^*, \mathbf{x}) \mathbf{K}(\mathbf{x}, \mathbf{x})^{-1} \Psi_f \quad (10)$$

where $\mathbf{k}(\mathbf{x}^*, \mathbf{x})$ is the vector of covariances between the new test point \mathbf{x}^* and the training data points \mathbf{x} . The matrix $\mathbf{K}(\mathbf{x}, \mathbf{x})$ is the covariance between all training inputs. The vector Ψ_f contains all the observations of the strain energy of the fibers for all the inputs \mathbf{x} . The posterior covariance is

$$\Sigma_f = \mathbf{K}(\mathbf{x}^*, \mathbf{x}^*) - \mathbf{k}(\mathbf{x}^*, \mathbf{x}) \mathbf{K}(\mathbf{x}, \mathbf{x})^{-1} \mathbf{k}(\mathbf{x}, \mathbf{x}^*). \quad (11)$$

Given the posterior GP for the strain energy, Ψ_f^* , the derivatives of the strain energy function with respect to the invariants are also GPs that can be easily computed from eqs. (12) and (11) [35]. The mean of the gradient of the GP is simply the derivative of the mean function (12),

$$\mu_{\Psi_i} = \mathbf{k}_i(\mathbf{x}^*, \mathbf{x}) \mathbf{K}(\mathbf{x}, \mathbf{x})^{-1} \Psi_f, \quad (12)$$

where $\mathbf{k}_i(\mathbf{x}^*, \mathbf{x})$ is the vector with the derivatives of the kernel $\partial k((I_1^*, I_2^*, \mathbf{x}) / \partial I_i^*$. The covariance of the derivatives can be obtained from the derivative of the kernel function,

$$\Sigma_{\Psi_i, \Psi_j} = \frac{\partial^2 k(\mathbf{x}, \mathbf{x}')}{\partial I_i \partial I_j'}. \quad (13)$$

However, the GPs for the derivative functions defined with eq. (12) ignore the stress information and rely solely on the energy information. Thus, we furthered constrained the derivatives of the strain energy based on the stress data. In the previous section, the stress for a nearly incompressible material was derived. This description was the one

that we eventually implemented in the finite element subroutine. In the RVE simulations incompressibility could be imposed exactly. For incompressible plane stress behavior the stress can be simplified to

$$\sigma = 2\mathbf{b} \frac{\partial \Psi_{\text{iso}}}{\partial \mathbf{b}} + p\mathbf{I} \quad (14)$$

with $\det(\mathbf{b}) = \det(\mathbf{F}^M) = 1$, and where p becomes a Lagrange multiplier that can be solved for to ensure the plane stress condition $\sigma_{zz} = 0$. Expanding the derivative of the strain energy in (14),

$$\sigma = 2\Psi_1(I_1, I_2)\mathbf{b} + 2\Psi_2(I_1, I_2)(I_1\mathbf{b} - \mathbf{b}^2) + p\mathbf{I}. \quad (15)$$

To summarize, from the set of RVE simulations a GP was constructed over the total strain energy of the fibers as a function of the invariants of the applied deformation. This GP ignored the stress data. However, a relationship between the stress and the derivatives of the strain energy is available as seen in eq. (15). Thus, an additional optimization was performed to correct the derivatives of the strain energy predicted by the GP in order to also satisfy (15). The pressure needed for the plane stress condition in the RVE was also computed during this optimization step. The optimization was carried out with the *minimize* function in the *optimization* module of the Python package SciPy [36]. At the end of this step we had all the data as illustrated in Figure 2A.

Fully connected neural network

Based on the previous steps, schematized in Figure 2A, the overall input data consisted of the variables $\{\lambda_x, \lambda_y, I_1, I_2, \theta, \varphi\}$, as well as multiple realizations of the networks even for the same $\{\theta, \varphi\}$. However, not all these inputs are independent. Ultimately, the goal was to obtain a model that was a function of the deformation invariants. Yet, it was easier to generate the training data by imposing the principal stretches. Thus, deformations on the RVE were imposed by sampling the in-plane stretches $\{\lambda_x, \lambda_y\}$ which were post-processed to get the invariants $\{I_1, I_2\}$. Similarly, the output consisted of the variables $\{\sigma, p, \Psi, \Psi_1, \Psi_2\}$. For a finite element implementation, only prediction of the functions $\{\Psi_1, \Psi_2\}$ is needed. Nevertheless, two FCNN were trained. A FCNN to predict the stress tensor directly as a function of the stretches λ_x, λ_y was trained. However, this approach imposes the choice of a cartesian coordinate system aligned with the principal in-plane directions for the strain and stress tensors. Therefore this network was not explored in much detail. An alternative approach, favored in this work, is to train the FCNN to predict the derivatives of the strain energy, Ψ_1, Ψ_2 , as function of the strain invariants. This second approach was the one implemented in the commercial finite element software Abaqus. In addition to the advantage of an invariant-based formulation, training the FCNN on the strain energy and its derivatives enabled the imposition of meaningful constraints, namely the convexity of the strain energy. The process of FCNN training is illustrated in Figure 2B.

For the FCNN trained to predict Ψ_1 and Ψ_2 , a weighted combination of the mean squared error (MSE) loss, mean absolute error (MAE) loss, and the mean absolute percentage error (MAPE) loss were used

$$\begin{aligned} \mathbb{L}_i^{\text{MSE}} &= \frac{1}{N} \sum_{n=1}^{\#data} \left(\Psi_i^{(n)} - \hat{\Psi}_i^{(n)} \right)^2 \\ \mathbb{L}_i^{\text{MAE}} &= \frac{1}{N} \sum_{n=1}^{\#data} \left| \Psi_i^{(n)} - \hat{\Psi}_i^{(n)} \right| \\ \mathbb{L}_i^{\text{MAPE}} &= \frac{100}{N} \sum_{n=1}^{\#data} \left| \frac{\Psi_i^{(n)} - \hat{\Psi}_i^{(n)}}{\Psi_i^{(n)}} \right| \end{aligned} \quad (16)$$

where $i = 1, 2$, n denotes each one of the N data pairs $\{(\varphi^{(n)}, \theta^{(n)}, I_1^{(n)}, I_2^{(n)}), (\Psi_1^{(n)}, \Psi_2^{(n)})\}$, and $\hat{\Psi}_i^{(n)}$ is the prediction of the strain energy derivative by the FCNN for the corresponding input $(\varphi^{(n)}, \theta^{(n)}, I_1^{(n)}, I_2^{(n)})$. The losses in (16) only penalize the error in the prediction of Ψ_1 and Ψ_2 . However, as mentioned previously, an advantage of assuming a hyperelastic framework is that physically realistic constraints can also be considered during training of the FCNN. Indeed, a major driver for the development of analytical expressions for strain energy potentials of soft tissue

is that convexity can be analyzed in detail [37]. For the FCNN, the Hessian matrix of the strain energy function can be computed numerically at any of the n inputs used for training,

$$\mathbf{H}^{(n)} = \begin{pmatrix} \Psi_{11} & \Psi_{12} \\ \Psi_{21} & \Psi_{22} \end{pmatrix} = \begin{pmatrix} \frac{\partial \hat{\Psi}_1^{(n)}}{\partial I_1} & \frac{\partial \hat{\Psi}_1^{(n)}}{\partial I_2} \\ \frac{\partial \hat{\Psi}_2^{(n)}}{\partial I_1} & \frac{\partial \hat{\Psi}_2^{(n)}}{\partial I_2} \end{pmatrix}. \quad (17)$$

The Hessian contains the second derivatives of the strain energy. On the other hand, since the FCNN output are already the first derivatives Ψ_1, Ψ_2 , only one derivative of the FCNN output is required. Computing the derivatives of the FCNN output with respect to the inputs is straightforward and follows an algorithm analogous to back-propagation [38]. The first obvious constraint on the FCNN output is that the Hessian must be positive. Therefore, one additional component of the loss is

$$\mathbb{L}^{\text{sym}} = \sum_{n=1}^{\#data} \left| \frac{\partial \hat{\Psi}_1^{(n)}}{\partial I_2} - \frac{\partial \hat{\Psi}_2^{(n)}}{\partial I_1} \right| \quad (18)$$

The second constraint is the positive semi-definiteness of \mathbf{H} which is enforced by the loss [39]

$$\mathbb{L}^{\text{psd}} = \frac{1}{N} \sum_{n=1}^{\#data} \left| \frac{\partial \Psi_1^{(n)}}{\partial I_1} \right| + \frac{1}{N} \sum_{n=1}^{\#data} \left| \frac{\partial \Psi_1^{(n)}}{\partial I_1} \frac{\partial \Psi_2^{(n)}}{\partial I_2} - \frac{\partial \Psi_1^{(n)}}{\partial I_2} \frac{\partial \Psi_2^{(n)}}{\partial I_1} \right| \quad (19)$$

Hence, the final loss function of the convexity constraints can be obtained by adding the different losses, each with a given weight. The weights were manually adjusted to obtain desired accuracy and satisfaction of the constraints. In particular, the effect of the weights of the symmetry constraint α^{sym} and of the positive semi-definiteness constraint α^{psd} were investigated in more detail in the Results section.

An additional FCNN for the prediction of the principal stresses as a function of the principal stretches was also constructed. However, since in the end this FCNN was not implemented into the finite element code, only the standard MAPE loss was used in training, which is a standard in machine learning [40, 41].

The Adam optimization algorithm [42] was used to train the networks and update the FCNN weights during back-propagation [43]. The initial learning rate was set as 0.0001 with a momentum decay of 0.9. The training and validation data splits were 85% and 15% of the total data points. The total number of observations was 132,000 for the 1,100 networks and the different deformations. A typical FCNN consists of an input layer, one or more hidden layers, and an output layer. Here we trained and evaluated an FCNN with 3 hidden layers of dimensions 8, 8, and 16 respectively, and 1 output layer. The activation function used was ReLu [44](Table 1). The training was implemented using Keras [45] with a TensorFlow [46] back-end on a hardware platform with the following specifications: Overclocking 5.0 GHz Intel i9 processor, 32 GB DDR4/2666 MHz memory, and Nvidia GeForce GTX 1080. The batch size, which controls the number of samples to be propagated through the network at a time was set as 64 to avoid local minima, enhance generalization performance, and improve the optimization convergence [47].

Table 1: NN architectures

Layer (type)	Output shape	# Parameters
Dense 1	8	40
Activation 1	8	0
Dense 2	8	72
Activation 2	8	0
Dense 3	16	144
Activation 3	16	0
Dense 4	2	34
Activation 4	2	0

Finite element implementation

A general FCNN-based user material subroutine (UMAT) was implemented in the nonlinear finite element package Abaqus Standard (Rhode Island, United States). Rather than hard-coding the specific FCNN that was trained on the DFN data, the UMAT function was programmed to take in the network architecture and the weights and biases as material parameters. Thus, the FCNN needs to be specified in the input file. As a result, the UMAT can be used for different FCNN architectures and trained on different data. In the UMAT function itself, the FCNN is constructed and evaluated based on the information of the input file. This approach gives flexibility. For example, in this paper two different regions in a finite element model were assigned different FCNNs to model their material behavior without the need for multiple user subroutines. The deformation gradient \mathbf{F} at an integration point is passed as one of the arguments of the UMAT. Based on this deformation gradient, the corresponding isochoric left Cauchy Green deformation, $\bar{\mathbf{b}}$, and its invariants \bar{I}_1, \bar{I}_2 , are computed. Then, using the microstructure parameters φ and θ which are defined as material properties, together with the network architecture and the weights and biases of the network (also defined as material properties), the FCNN evaluates Ψ_1, Ψ_2 . Evaluation of neural networks is a combination of simple operations. Consider a dense layer, layer i , of the network. Layer i takes in m inputs from the previous layer stored in vector \mathbf{y}_{i-1} and produces n outputs \mathbf{y}_i . In other words, m is the number of neurons in layer $i-1$ and n is the number of neurons in the layer i . The weights for this layer are arranged in the matrix \mathbf{W}_i which is $m \times n$. The vector of biases for layer i is denoted \mathbf{B}_i . Propagation of information in this layer corresponds to the linear map

$$\mathbf{y}_i = \mathbf{W}_i^T \mathbf{y}_{i-1} + \mathbf{B}_i. \quad (20)$$

The nonlinearity in the network comes from the activation layers. For the activation layer i , the output is simply

$$\mathbf{y}_i = g(\mathbf{y}_{i-1}) \quad (21)$$

where $g(\bullet)$ is the activation function applied element-wise to the vector \mathbf{y}_{i-1} . The ReLu activation function used here is $g(y) = \max(0, y)$. In addition to computing the functions Ψ_1, Ψ_2 , their derivatives with respect to the invariants \bar{I}_1, \bar{I}_2 are needed for the elasticity tensor, which is essential for the convergence of the Newton iterations of the finite element solver. For a dense layer i , the input gradient is \mathbf{J}_{i-1} of dimension $m \times n_{\text{input}}$, with n_{input} the number of inputs to the whole FCNN. The gradient output of a dense layer i is

$$\mathbf{J}_i = \mathbf{W}_i^T \mathbf{J}_{i-1}. \quad (22)$$

For the activation layer, the gradient output is

$$\mathbf{J}_i = \text{diag}(g'(\mathbf{y}_i)) \mathbf{J}_{i-1}. \quad (23)$$

where $\text{diag}(\bullet)$ denotes a diagonal matrix, and $g'(\bullet)$ is the derivative of the activation function. The gradient for the input layer is initialized as the identity matrix of size $n_{\text{input}} \times n_{\text{input}}$. After doing the operations defined in (22) and (23), the gradient output is a matrix of size $n_{\text{output}} \times n_{\text{input}}$. For the particular FCNN used in this paper, the final gradient output contains the Hessian (17) as a sub-matrix.

After evaluation of the FCNN, the prediction of Ψ_1 and Ψ_2 are used to compute the isochoric stress based on equations (8) and (9). Additionally, a volumetric strain energy is required, which is not part of the FCNN prediction. Here we opt for a classical expression for the volumetric part of the strain energy

$$\Psi_{\text{vol}} = \frac{K}{2} (J - 1)^2 \quad (24)$$

where K is the bulk modulus and $J = \det(\mathbf{F})$ is the volume change.

The consistent tangent can be derived independently of the material model, simply by knowing the second derivatives of the strain energy function. The FCNN outputs the prediction of the second derivatives based on the operations

(22) and (23) . The following terms are used for ease of notation of the consistent tangent

$$\begin{aligned}\delta_1 &= 4(\Psi_2 + \Psi_{11} + 2\bar{I}_1^2\Psi_{22}) \\ \delta_2 &= -4(\Psi_{12} + \bar{I}_1\Psi_{22}) \\ \delta_3 &= 4\Psi_{22} \\ \delta_4 &= -4\Psi_2\end{aligned}\tag{25}$$

where $\Psi_{11}, \Psi_{12}, \Psi_{21}, \Psi_{22}$ are the derivatives predicted by the FCNN that correspond to the entries of the Hessian, eq. (17). The isochoric part of the elasticity tensor is

$$\begin{aligned}J\mathbb{C}_{\text{mathrm{miso}}} = & \delta_1 \left(\bar{\mathbf{b}} \otimes \bar{\mathbf{b}} - \frac{1}{3}\bar{I}_1(\bar{\mathbf{b}} \otimes \mathbf{I} + \mathbf{I} \otimes \bar{\mathbf{b}}) + \frac{1}{9}\bar{I}_1^2\mathbf{I} \otimes \mathbf{I} \right) \\ & + \delta_2 \left(\hat{\mathbf{b}} \otimes \bar{\mathbf{b}}^2 + \bar{\mathbf{b}}^2 \otimes \bar{\mathbf{b}} - \frac{1}{3}\text{tr}(\bar{\mathbf{b}}^2)(\bar{\mathbf{b}} \otimes \mathbf{I} + \mathbf{I} \otimes \bar{\mathbf{b}}) - \frac{1}{3}\bar{I}_1(\bar{\mathbf{b}}^2 \otimes \mathbf{I} + \mathbf{I} \otimes \bar{\mathbf{b}}^2) + \frac{2}{9}\bar{I}_1\text{tr}(\bar{\mathbf{b}}^2)\mathbf{I} \otimes \mathbf{I} \right) \\ & + \delta_3 \left(\bar{\mathbf{b}}^2 \otimes \bar{\mathbf{b}}^2 - \frac{1}{3}\text{tr}(\bar{\mathbf{b}}^2)(\bar{\mathbf{b}}^2 \otimes \mathbf{I} + \mathbf{I} \otimes \bar{\mathbf{b}}^2) + \frac{1}{9}(\text{tr}(\bar{\mathbf{b}}^2))^2\mathbf{I} \otimes \mathbf{I} \right) \\ & + \delta_4 \left(\bar{\mathbf{b}} \bar{\otimes} \bar{\mathbf{b}} - \frac{1}{3}(\bar{\mathbf{b}}^2 \otimes \mathbf{I} + \mathbf{I} \otimes \bar{\mathbf{b}}) + \frac{1}{9}(\bar{\mathbf{b}} : \bar{\mathbf{b}})\mathbf{I} \otimes \mathbf{I} \right)\end{aligned}\tag{26}$$

where the following special dyadic product was used $(\bullet)_{ij}\bar{\otimes}(\circ)_{kl} = (\star)_{ikjl}$. The volumetric contribution of the elasticity tensor is

$$\mathbb{C}_{\text{vol}} = \left(p + J \frac{\partial p}{\partial J} \right) \mathbf{I} \otimes \mathbf{I} - 2p\mathbf{I} \bar{\otimes} \mathbf{I}.\tag{27}$$

The isochoric and volumetric components of the spatial elasticity tensor defined in eqs. (26) and (27) are part of the consistent tangent needed for Abaqus' Newton-Raphson solver. Mechanical equilibrium is solved in Abaqus by incrementally integrating the stress using the Jaumann stress rate. As a result, the consistent tangent needs a correction with respect to the standard form of the elasticity tensor [48]. The tangent for Abaqus takes the form

$$\mathbb{C}_{\text{abaqus}} = \mathbb{C}_{\text{iso}} + \mathbb{C}_{\text{vol}} + \frac{1}{2}(\sigma \bar{\otimes} \mathbf{I} + \sigma \underline{\otimes} \mathbf{I} + \mathbf{I} \bar{\otimes} \sigma + \mathbf{I} \underline{\otimes} \sigma)\tag{28}$$

in which an additional tensor product is defined as $(\bullet)_{ij}\bar{\otimes}(\circ)_{kl} = (\star)_{iljk}$. In summary, the architecture, weights, and biases of the FCNN are passed to the UMAT subroutine as material parameters, and the FCNN is evaluated given the current deformation gradient at an integration point to output Ψ_1, Ψ_2 and their derivatives $\Psi_{11}, \Psi_{12}, \Psi_{21}, \Psi_{22}$. These functions are used to compute the stress σ and the consistent tangent $\mathbb{C}_{\text{abaqus}}$.

Results

Response under uniaxial and biaxial loading

We first compared that the results from our DFN implementation matched observations from previous computational models of fiber networks as well as experimental data on fibrin gels. We created 110 networks with a volume fraction $\theta \approx 0.3\%$, $\theta \in (0.297\%, 0.303\%)$ and fiber diameter $\varphi = 100\text{nm}$. The volume fraction could not be controlled exactly because the networks were generated by seeding the RVE with randomly located nucleation points and letting them grow in random directions until the algorithm was terminated. Due to these sources of randomness, control of the exact fiber length was not possible. Nevertheless, the range of volume fractions obtained was very close to the desired value of 0.3%. We created multiple networks with the same values θ and φ because these variables describe the homogenized network properties but do not specify a network uniquely.

The 110 RVEs were subjected to uniaxial deformation following similar approaches in the literature [49, 29, 7]. The nonlinear relationship of stress as a function of stretch was observed, with increasing slope at higher stretch

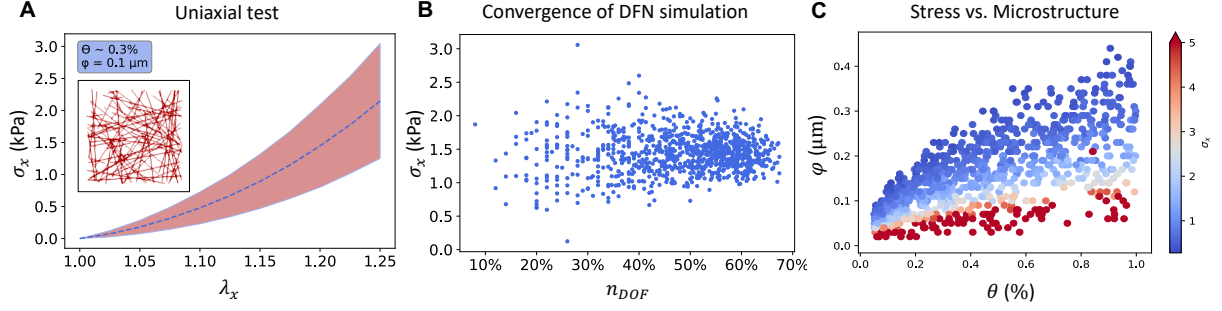


Figure 3: Verification of DFN response under uniaxial deformation. In uniaxial tests (A), 110 networks with homogenized microstructure properties $\theta \approx 0.3\%$, $\varphi = 100\text{nm}$ showed nonlinear behavior. Even though the networks shared the same homogenized properties θ , φ , the random nature of the networks leads to uncertainty in the predicted stress σ_x , shown as a shaded area (A). The variance in the stress σ_x was dependent on the number of degrees of freedom of the network, defined as the percentage of inner nodes with respect to total number of nodes (B). The stress in uniaxial tests was a function of the homogenized microstructure properties φ and θ for a fixed value of fiber stiffness, with increasing stress for smaller fiber diameters and relatively little influence of the volume fraction (C).

values. At a stretch of $\lambda_x = 1.2$, for example, the mean (+/- S.D.) stress was $1.45 \text{ kPa} \pm 0.33 \text{ kPa}$ (Figure 3A). The stress showed variance, suggesting that even networks with the same homogenized microstructure properties φ , θ , can have slightly different mechanical behavior. To further explore this uncertainty, we plotted the variance in the stress as a function of the relative number of degrees of freedom, i.e. the number of inner nodes with respect to the total number of nodes (Figure 3B). Decreased variance with higher number of degrees of freedom was observed. Variation of the microstructure variables θ , φ , led to consistent trends in the stress response under uniaxial deformation: decreasing fiber diameter led to increase in stress, almost independently of volume fraction (Figure 3C). We note that the stiffness k_f was kept constant (0.02 kPa), independent of fiber diameter.

The response of the networks under biaxial deformations was also explored. Figure 4 shows the response under off-biaxial testing keeping $\lambda_y = 1$. For the 110 networks with $\theta = 0.3\%$, $\varphi = 100\text{nm}$, the strain energy density in the fibers, Ψ , showed a similar trend to the uniaxial tests. The strain energy increased nonlinearly for increasing stretch, with some variance attributed to the randomness of the 110 networks even though they shared the same homogenized properties (Figure 4A). We also explored the effect of the number of degrees of freedom on the variance of the strain energy. A slight decrease in the variance of Ψ could be found as the number of degrees of freedom increased (Figure 4B), although this was less obvious compared to the stress response. Analyzing the mechanical behavior with respect to the microstructure variables, it can be seen that low volume fraction and smaller diameters resulted in higher energy density (Figure 4B). The derivatives, Ψ_1 and Ψ_2 , showed a slightly nonlinear response with a relatively constant variance with respect to the deformation. The variance in the derivatives did not show a strong dependence on the number of degrees of freedom (Figure 4E,H). Analyzing the contours of the functions Ψ_1 and Ψ_2 , it can be seen that they depend on the microstructure variables θ and φ in a similar way to the stress (Figure 4F,I), which is expected since these derivatives appear linearly in the definition of the stress tensor, see eq. (15). Note that for a neo-Hookean material, the value of Ψ_1 will be a constant and the value of Ψ_2 will be zero. For a Mooney-Rivlin material, the value of both Ψ_1 and Ψ_2 will be non-zero constants. Our results show that the DFN networks are slightly more nonlinear than these simple but commonly used strain energy functions. Instead of trying to find an analytical expression with a higher degree of nonlinearity to match the data, the next section explains how the FCNN was trained to predict the mechanical response without the need of classical strain energy functions.

FCNN training and validation

A total of 132,000 data points were used to train the FCNN with the architecture specified in Table 1. Traditionally, a single loss function is used for the optimization of the weights and biases of the FCNN. However, as outlined above, to obtain strain energies that satisfied convexity with respect to the deformation invariants, multiple loss functions were linearly combined. In particular, there was a trade-off between the weights assigned to the loss functions that drove the accuracy of the predictions and the weights assigned to the loss functions that drove the convexity and symmetry constraints. A grid search was performed to select the weights α^{psd} and α^{sym} , which enforced the positive

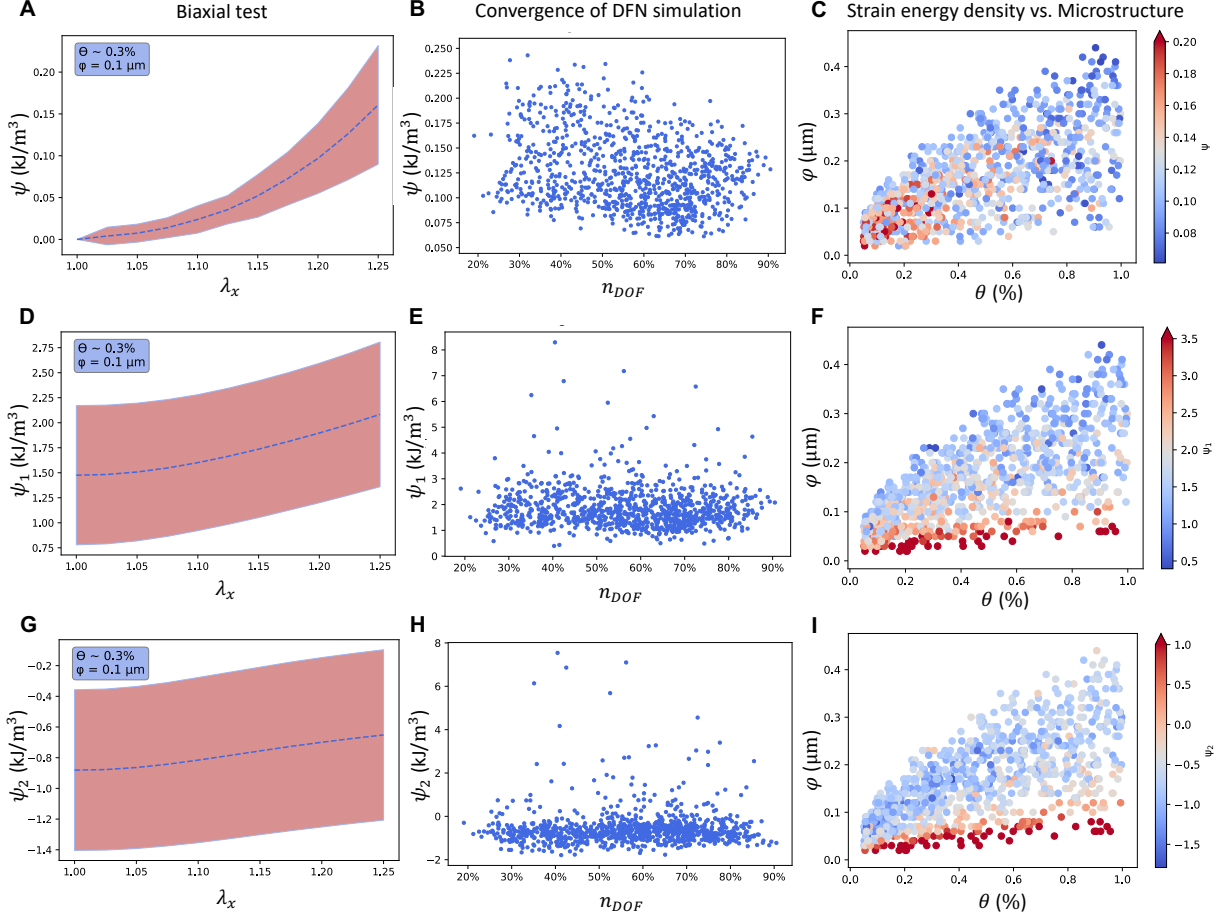


Figure 4: Response of DFNs under off-biaxial loading. The strain energy Ψ (A), and its derivatives Ψ_1 , Ψ_2 show a nonlinear response with respect to increasing deformation (D, G). The strain energy variance depends on the number of degrees of freedom (B), while the derivatives are relatively constant even as the number of degrees of freedom increases (E, H). In response of changes in microstructure, the strain energy in the fibers increases with both volume fraction θ and fiber diameter φ (C), while the derivatives Ψ_1 and Ψ_2 are mostly insensitive to the volume fraction but increase with fiber diameter (F, I).

definiteness and symmetry conditions, respectively. Performance within 500 training epochs was used to examine the effect of these parameters. The results for grid search on the accuracy with respect to the change in these weights is shown in Table 2. This table clearly shows the trade off between the accuracy and the convexity of the model. Once α^{psd} and α^{sym} were large enough, further increase only produced minor changes in the convexity loss. The set of weights $\alpha^{\text{psd}} = \alpha^{\text{sym}} = 10^4$ was selected since it yielded an overall good validation accuracy while satisfying the convexity condition. Finally, a model with a total loss of 70.26 was achieved. The MAPE loss for Ψ_1 was 26.05, the MSE loss for Ψ_1 was 0.91, and the MAE loss for Ψ_1 was 0.50. For Ψ_2 , due to predictions close to zero, only the weight associated to the MAE loss was considered, and the value of this loss function for Ψ_2 was 0.38 in the final model. The positive definiteness loss was $1.35\text{E-}10$, and the symmetry loss $2.32\text{E-}05$.

Table 2: FCNN performance for the grid search over the parameters $\alpha^{\text{sym}}, \alpha^{\text{psd}}$.

α^{sym}	α^{psd}	$\sum \mathbb{L}$	\mathbb{L}_{MAPE}	\mathbb{L}_{MSE}	\mathbb{L}_{MAE}	\mathbb{L}_{MAE}	\mathbb{L}_{psd}	\mathbb{L}_{sym}
0.	1.	49.41	21.76	0.20	0.33	0.24	4.39	3.44
1.	1.	57.81	24.59	0.64	0.38	0.28	0.30	0.24
10^2	1.	67.97	31.30	2.20	0.67	0.27	8.39×10^{-4}	0.057
10^2	10^2	68.23	31.44	2.14	0.67	0.27	5.95×10^{-4}	0.002
10^4	10^2	70.39	29.86	1.39	0.60	0.33	5.45×10^{-10}	4.57×10^{-5}
10^4	10^4	70.26	26.05	0.91	0.50	0.38	1.35×10^{-10}	2.32×10^{-5}
10^6	10^4	74.66	26.27	0.92	0.50	0.42	4.36×10^{-9}	5.09×10^{-6}
10^6	10^6	76.70	28.23	0.98	0.53	0.42	1.4×10^{-17}	6.63×10^{-9}

A second FCNN was trained, using the same overall data, but in this case the inputs were the principal stretches λ_x and λ_y , and the outputs were the components of the stress tensor σ . This FCNN was not used in the finite element implementation, but it was useful for evaluating the ability of the FCNN approach to capture the mechanical response of the DFNs. For the FCNN that was trained to predict the stress tensor, only the MAPE loss function was used, as described in the Methods section. No constraints were considered in this case. The final loss for this FCNN was 12.72%.

As seen in the uniaxial and biaxial response tests (Figures 3 and 4), even for the same microstructure variables θ and φ , there is variance in the stress, the strain energy, and the derivatives of the strain energy. The FCNN trained on stress data was first compared to strip-biaxial data from 60 DFNs with the equivalent microstructure $\theta = 0.3\%$, $\varphi = 100\text{nm}$. Figure 5A shows the comparison of the FCNN prediction of the stress against the mean response of the 60 DFNs. The microstructure variables for this case, $\theta = 0.3\%$, $\varphi = 100\text{nm}$, were not part of the training. We found that the FCNN predictions (red solid line) laid well within the confidence interval (blue shading) and were very close to the mean value of the simulations of the 60 DFNs (blue dashed line in Figure 5A). During training, the raw data from each DFN was used, and not the mean response of different DFNs. The loss functions were evaluated with respect to the raw DFN data, i.e. without taking into account the variance in the DFN response. Thus, the FCNN converged naturally toward the mean response with respect to the microstructure variables even though it was not trained directly on the mean data from multiple RVEs with the same θ, φ . To explore the error as a function of microstructure, additional testing data consisting of 1000 simulations with different combinations of θ and φ were evaluated under strip-biaxial loading. The results are shown in Figure 5B. In this case, the prediction of the FCNN was compared against at least 20 fiber networks sharing equivalent θ, φ pairs that were not a part of the training data.

The FCNN that was trained directly on the derivative data Ψ_1 and Ψ_2 was first compared to 100 DFNs with the equivalent microstructure $\theta = 0.3\%$, $\varphi = 100\text{nm}$, subjected to strip-biaxial loading. The DFNs in the validation set were separated based on the number of seeds used to initialize the networks, which is related to the number of fibers in the network. Individual validation data (dashed lines) shows higher nonlinearity than the FCNN prediction (solid lines). Nevertheless, the FCNN prediction was inside of the confidence intervals (shaded areas) of the DFNs (Figure 5C,E). The reason for the flattening of the FCNN prediction is the imposition of the convexity constraints, which lead to predictions within the confidence interval while preserving convexity in the entire input space. Relaxation of the convexity constraints leads to more accuracy with respect to individual curves in the validation set, but compromises the convexity constraint which is no longer satisfied everywhere. As a function of the microstructure variables θ and φ , the model predicted Ψ_1, Ψ_2 with small errors for most networks (Figure 5D,F).

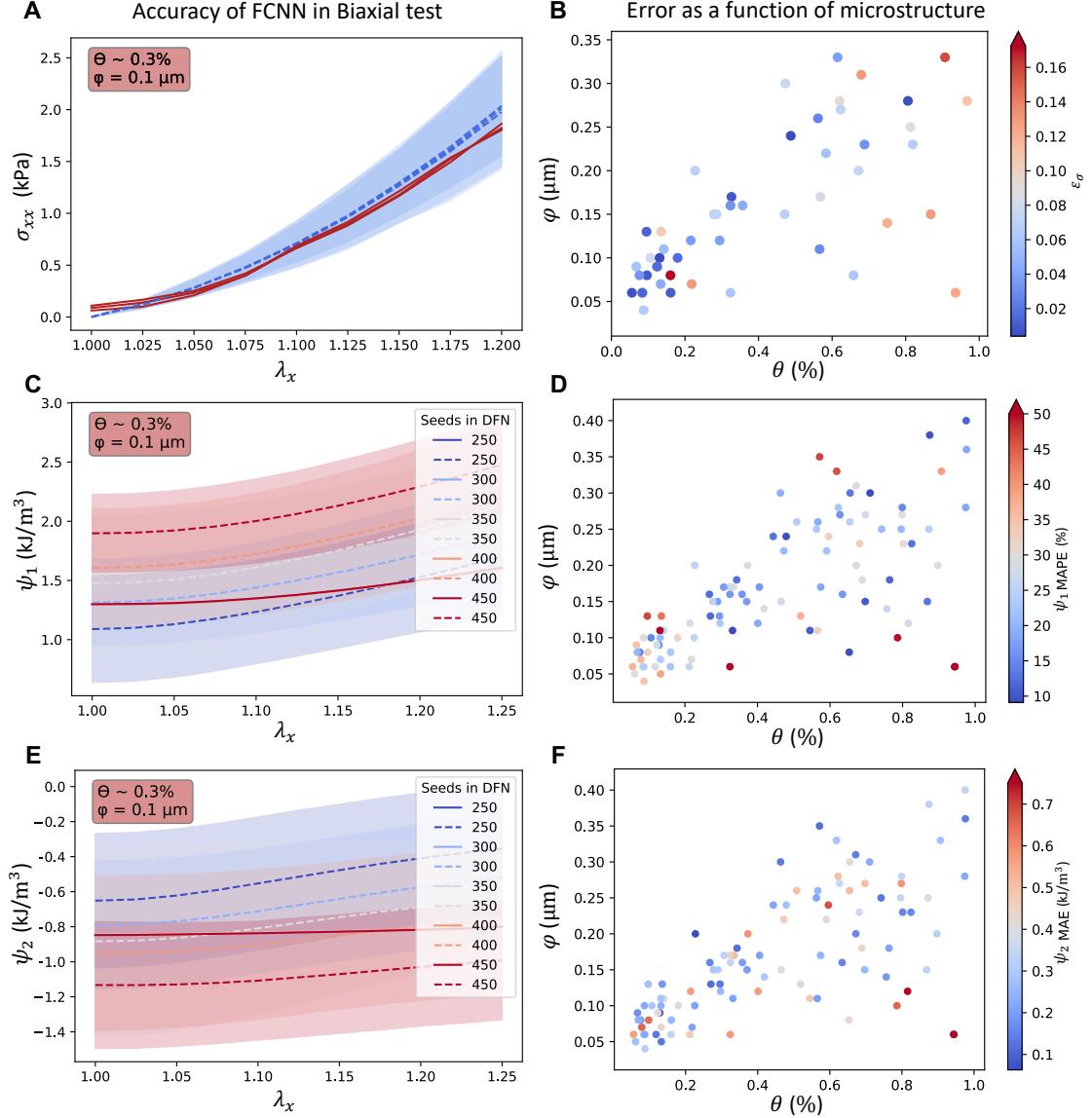


Figure 5: Performance of the FCNN against the testing set. Performance of a neural network for the prediction of stress in strip biaxial loading (solid red line) for showed agreement with the mean (dashed blue line) and confidence interval (shaded blue region) of 60 DFNs with the equivalent microstructure microstructure $\theta = 0.3\%$, $\varphi = 100\text{nm}$ (A). Error as a function of microstructure showed less accuracy of the FCNN for larger volume fractions and fiber diameters (B). The derivatives of the strain energy predicted by the FCNN (solid red lines) also agreed with the means (dashed lines) and confidence intervals (shaded regions) of DFNs with equivalent microstructure (C,E). The variance in the ground truth was affected by the number of fibers in the network. Loss function values for Ψ_1 and Ψ_2 did not show a distinctive trend as a function of microstructure (D,F).

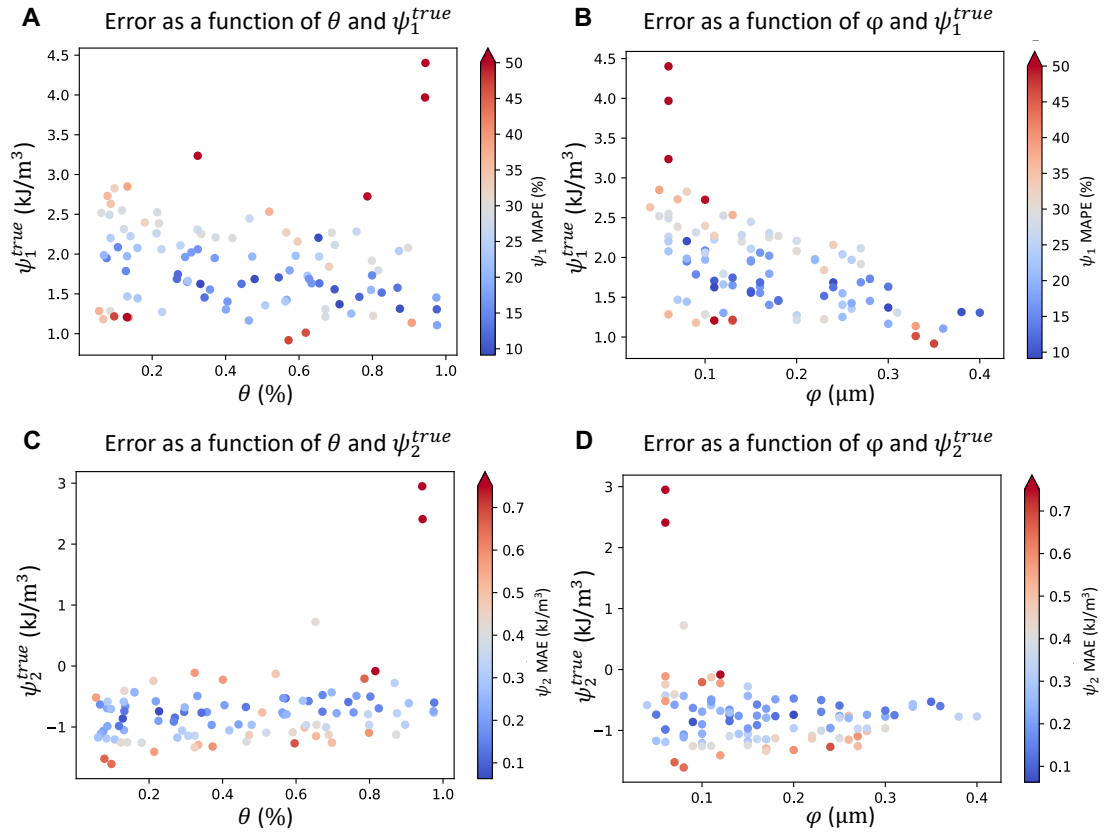


Figure 6: Performance of the FCNN as a function of microstructure. Predictions of the derivative function Ψ_1 with respect to the volume fraction θ (A) and the fiber diameter φ (B). The error of the second derivative prediction Ψ_2 showed similar trends with respect to θ and φ (C,D).

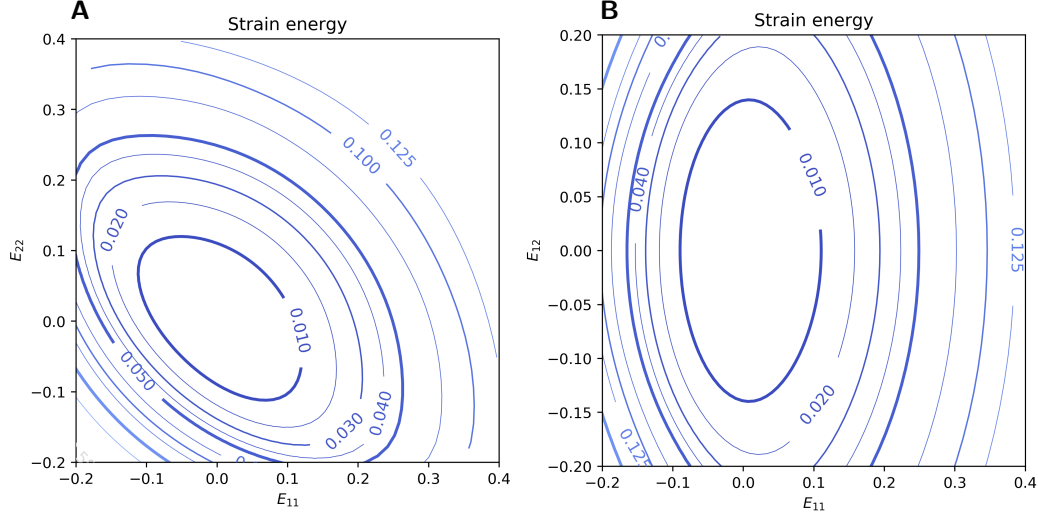


Figure 7: Strain energy density function with respect to E_{11} and E_{22} with $E_{12} = 0$ for a network with microstructure ($\theta = 0.3\%$, $\varphi = 100\text{nm}$) (A), and with respect to E_{11} and E_{12} with $E_{22} = 0$ (B).

Figure 6 further shows the dependence of the error on the microstructure while also showing the dependence on the true value of the derivative. Higher errors were seen on the edge of the plot, namely, for those networks with extreme volume fractions and fiber diameters. While most of the values for Ψ_1, Ψ_2 were small and concentrated within a narrow range, some outlier values were noticed at the ends of the ranges for volume fraction and fiber diameter (Figure 6). As expected, the FCNN metamodel predictions were better on the region of the output space closer to the center of the range spanned by the true Ψ_1 and Ψ_2 .

To visualize the convexity of strain energy density function from our FCNN, the strain energy density Ψ was computed over the strain space E_{11}, E_{22} , i.e. biaxial loading, as well as in the space E_{11}, E_{12} , which includes shear. The FCNN outputs the derivatives Ψ_1, Ψ_2 which were used to determine the second Piola Kirchhoff stress and integrated over strain curves $\int \mathbf{S} : d\mathbf{E}$. The resulting strain energy function contours computed in this manner were plotted and examined for a represented microstructure $\theta = 0.3\%$, $\varphi = 100\text{nm}$. The strain energy density function was convex, as expected from the imposition of the constraint (Figure 7).

Finite element simulation

Figure 8 shows results from three basic tests done to verify the correct implementation of the FCNN in the UMAT subroutine. We first performed a uniaxial test in which symmetry for X, Y, and Z planes was imposed on the corresponding boundaries. X-displacement was applied on one end of the domain to impose an overall stretch of $\lambda_x = 1.1$. The microstructure parameters used corresponded to $\varphi = 0.16\mu\text{m}$ and $\theta = 0.45\%$. The result is a homogeneous stress distribution that is required based on the boundary conditions, and it aligns with the FCNN calculation outside of the UMAT, $\sigma_{11} = 0.34\text{ kPa}$. Secondly, a uniaxial deformation for a higher stretch of $\lambda_x = 1.2$ was applied, but in this case, one of the ends was clamped. All other surfaces were traction-free. The finite element simulation converged without problems. In this case, due to the clamped boundary condition on one end, the stress distribution is no longer uniform and boundary effects are visible. The center point of the mesh still behaves correspondingly to uniaxial loading, with a stress that aligns with FCNN predictions. This simulation further suggests that the UMAT was implemented correctly. One last test was performed to verify that the simulation converged under different loading, in particular one that involves shearing. In this third simulation, the left end was kept clamped, but a shear deformation was added on the right boundary. All other surfaces were still traction free. The simulation converged also without a problem, and the resulting stress distribution showed a band of shear and normal stress along the diagonal, in agreement with the overall pattern of stress that would be expected from popular strain energy functions such as the neo-Hookean model. These results suggest that the FCNN was implemented correctly in the UMAT, that the second derivatives obtained through back-propagation are also implemented correctly in the UMAT, and that the potential satisfies convexity leading to the proper convergence of the simulation.

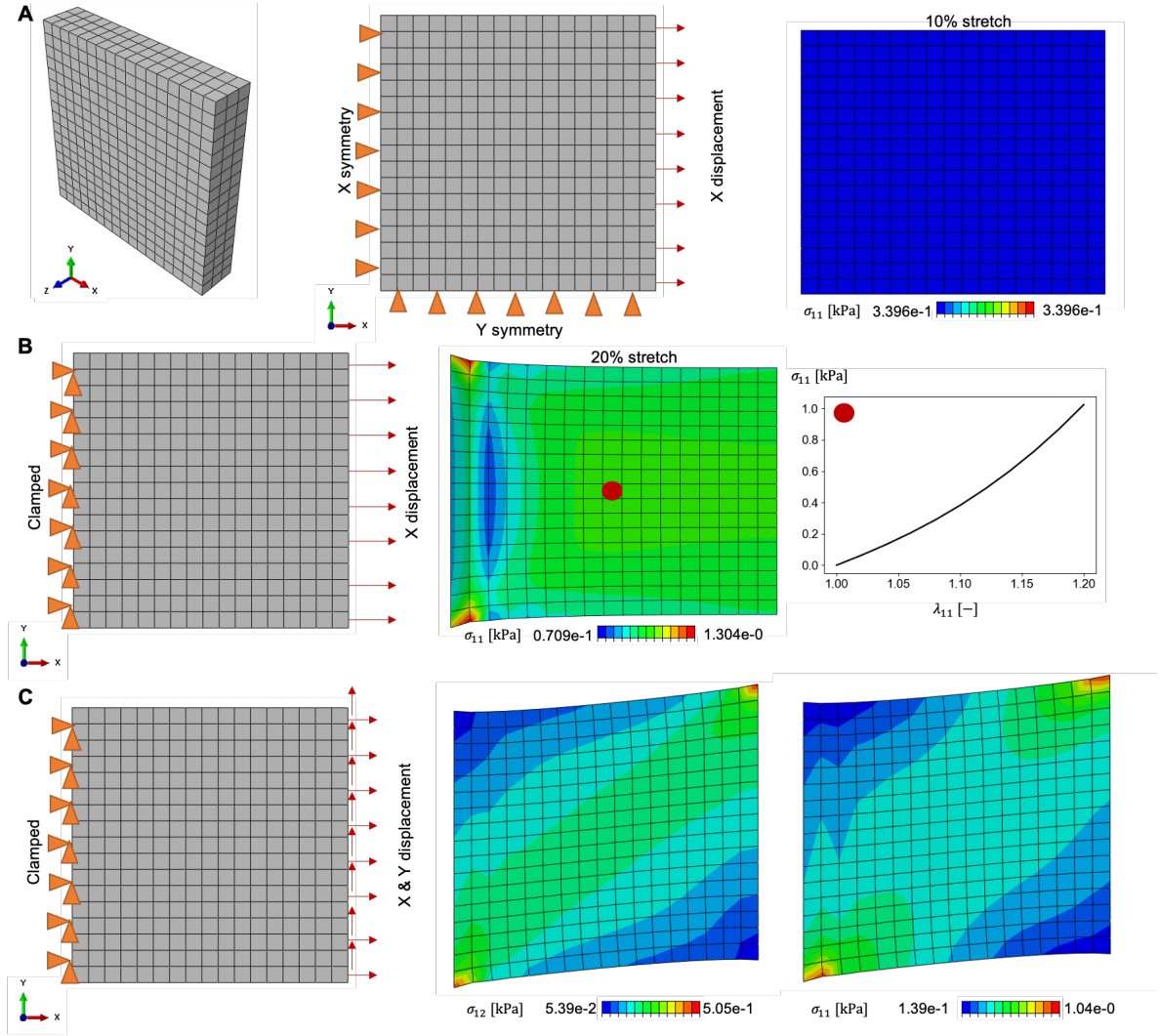


Figure 8: Finite element results using the FCNN in the UMAT subroutine. Uniaxial simulation with symmetry boundary conditions on the left and bottom boundaries leads to a uniform stress field (A). Clamping the left boundary leads to a non-uniform stress distribution; the center of the domain still behaves as in uniaxial loading (B). Shear simulations lead to a band of shear stress (C).

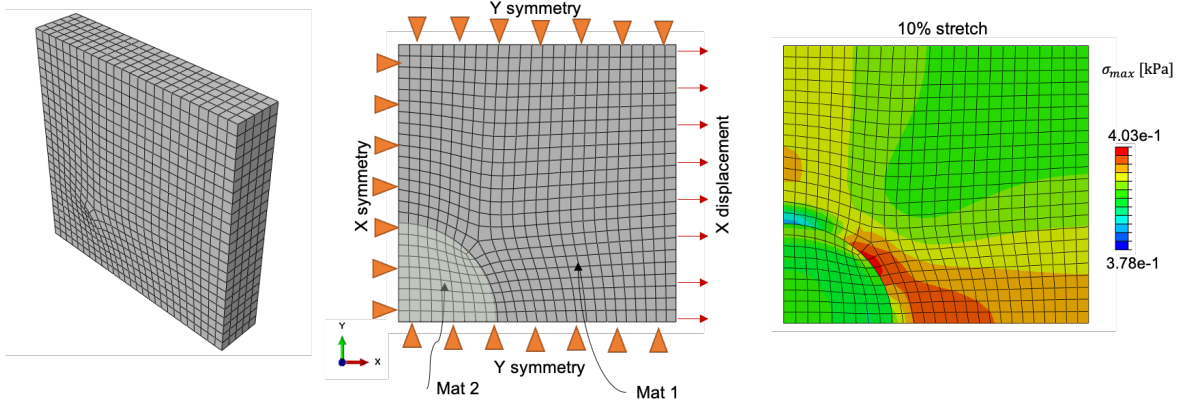


Figure 9: Finite element simulation of a rectangular domain with an inner region made out of a material with microstructure $\varphi = 0.02\mu\text{m}$ and $\theta = 0.05\%$ and a surrounding material defined by $\varphi = 0.5\mu\text{m}$ and $\theta = 0.99\%$. Due to symmetry at the bottom and left, only a quarter of the domain is modeled. The right surface was subjected to uniaxial deformation. Maximum principal stress is shown.

One final example was the modeling of a problem more representative of an application of this kind of material model. We modeled a quarter of a domain in which the center was made out of a different material with respect to the surrounding domain. This type of domain could represent a wound or a heterogeneous thrombus depending on the relative material properties. To model only a quarter of the domain, symmetry boundary conditions were used at the bottom and left surfaces, while the top surface has only Y fixed. The right surface was subjected to a uniaxial stretch. The UMAT was used for both domains, but with different inputs for the microstructure variables. For the surrounding material we used $\varphi = 0.5\mu\text{m}$ and $\theta = 0.99\%$, while for the interior circular domain the microstructure variables were set to $\varphi = 0.02\mu\text{m}$ and $\theta = 0.05\%$. The simulation results are shown in Figure 9, which shows the maximum principal stress over the entire domain. The microstructure of the inner domain corresponds to slightly softer material behavior of this inclusion, and similar to the Eshelby problem, the stress in the inclusion is nearly constant. The stress in the surrounding stiffer material is higher compared to the inner soft inclusion.

Discussion

In this study, we proposed to use a FCNN metamodel to replace a microscale fiber network model. The FCNN was trained on network microstructures subjected to a wide set of deformations. While the microscale model takes approximately 1 min to solve for equilibrium of a DFN, the prediction from the FCNN is obtained in less than 1msec, highlighting the significant speed-up from using machine learning tools to interpolate physics-based models. Significantly, the FCNN model has a simple structure with a small number of parameters and the metamodel can be constrained to satisfy physically meaningful equations, yielding an efficient and numerically stable finite element implementation. Moreover, the FCNN was trained on many different networks that span different microstructures in terms of volume fraction θ and fiber diameter φ . These constitutive parameters are physically relevant and can be defined by imaging experimentally-generated fibrin gels, when available. One version of the metamodel was trained to predict the stress as a function of the principal stretches and performed well in terms of relative error computed with respect to a testing data set. However, in order to achieve an invariant-based formulation, a FCNN to directly predict the derivatives of the strain energy with respect to the deformation invariants, Ψ_1 and Ψ_2 , was also trained.

The error of the FCNN against the validation data was due in part to the inherent uncertainty in the response of the DFNs. Even when the homogenized microstructure variables θ, φ , are fixed, this does not mean that the networks are fully determined. In practice, the networks were generated by seeding a domain with random nucleation points for fiber formation. Hence, this source of randomness leads to variance in the mechanical response for a given pair θ, φ . The type of FCNN used here is a deterministic model. When trained on the data from the different DFNs, the FCNN naturally learns the mean response for a given microstructure. Future work will use Bayesian neural networks that can capture the variance in the response instead of deterministic predictions [50, 51]. For those samples with

relatively larger error, the networks had extreme values of microstructure parameters. Moreover, some values of Ψ_1 , Ψ_2 in the validation set also had outliers at the edges of the parameter range. These unusual and inconsistent values compared to the rest of the training and validation data could be caused by the existence of non-unique solutions to the problem of fitting a GP and optimizing it to produce the derivative values. Other refinements of the DFN model can be considered. In this effort, we opted for a mechanical equilibrium problem in which fibers contribute only due to stretching but not bending. To make the networks more stable, bending resistance could be considered [52, 53]. Different constitutive models for individual fibers can also be incorporated [54, 9, 55, 1]. Another source of error in the FCNN prediction was the imposition of the convexity and symmetry constraints. The FCNN without this constraint more closely followed the data, but had small fluctuations in the response that led to loss of positive-definiteness locally. The constraint loss yielded a FCNN that satisfied these requirements, and while the predictions were well within the confidence intervals of the validation set, they appeared to be less nonlinear than the true values. Therefore, in addition to the Bayesian approach to handle the variance in the response function, networks with a more advanced structure and activation functions can also be considered in the future to improve the training and testing performance while still satisfying the symmetry and convexity requirements.

Due to the substantial reduction in computational time and good accuracy in the energy prediction, we embedded our FCNN as a user material subroutine in the commercial finite element package Abaqus. The finite element implementation showed that the FCNN led to stably convergent simulations. An advantage of our implementation is that the entire FCNN can be passed in a vector of material parameters defined in the input file. In this way, the UMAT does not evaluate the specific FCNN trained with the microscale mechanics data and can actually be used to evaluate any FCNN specified in the input file. For example the recent work by [56] shows that a FCNN can be used to interpolate heart valve biaxial data. The metamodel in [56] was not used in finite element simulations, however, due to the generality of our UMAT, the FCNN in [56] could be easily evaluated within our UMAT. All the files for this manuscript are available online.

Conclusions

Our work demonstrates that neural networks can be trained by micromechanical simulations, which capture ECM network behaviors and their relation to microstructural variables such as volume fraction and fiber diameter. The computational efficiency of this kind of machine learning metamodel makes it suitable for implementation within finite element simulations. More importantly, the FCNN relies on the data of the microscale model and not on any sort of analytical approximation. Future work includes using the FCNN to predict rate-dependent constitutive relations and for inverse estimation of microstructure parameters from a combination of mechanical tests and imaging data.

Acknowledgements

This work was supported in part by the National Science Foundation under grant No. 1911346-CMMI to PIs Tepole and Calve and the Bilsland Dissertation Fellowship to Dr. Yue Leng.

References

- [1] E. A. Sander, T. Stylianopoulos, R. T. Tranquillo, V. H. Barocas, Image-based biomechanics of collagen-based tissue equivalents, *IEEE engineering in medicine and biology magazine* 28 (2009) 10–18.
- [2] V. K. Lai, C. R. Frey, A. M. Kerandi, S. P. Lake, R. T. Tranquillo, V. H. Barocas, Microstructural and mechanical differences between digested collagen–fibrin co-gels and pure collagen and fibrin gels, *Acta biomaterialia* 8 (2012) 4031–4042.
- [3] A. Mol, M. I. van Lieshout, C. G. Dam-de Veen, S. Neuenschwander, S. P. Hoerstrup, F. P. Baaijens, C. V. Bouten, Fibrin as a cell carrier in cardiovascular tissue engineering applications, *Biomaterials* 26 (2005) 3113–3121.
- [4] G. Schlag, H. Redl, M. Turnher, H. Dinges, The importance of fibrin in wound repair, in: *Fibrin sealant in operative medicine*, Springer, 1986, pp. 3–12.
- [5] N. Laurens, P. d. Koolwijk, M. De Maat, Fibrin structure and wound healing, *Journal of Thrombosis and Haemostasis* 4 (2006) 932–939.
- [6] Y. Li, H. Meng, Y. Liu, B. P. Lee, Fibrin gel as an injectable biodegradable scaffold and cell carrier for tissue engineering, *The Scientific World Journal* 2015 (2015).
- [7] T. Stylianopoulos, V. H. Barocas, Volume-averaging theory for the study of the mechanics of collagen networks, *Computer methods in applied mechanics and engineering* 196 (2007) 2981–2990.

- [8] Y. Li, W. Chen, H. Xu, X. Jin, 3D representative volume element reconstruction of fiber composites via orientation tensor and substructure features, Technical Report, Ford Motor Company, 2016.
- [9] M. Hadi, E. Sander, J. Ruberti, V. H. Barocas, Simulated remodeling of loaded collagen networks via strain-dependent enzymatic degradation and constant-rate fiber growth, *Mechanics of materials* 44 (2012) 72–82.
- [10] B. Agoram, V. H. Barocas, Coupled macroscopic and microscopic scale modeling of fibrillar tissues and tissue equivalents, *J. Biomech. Eng.* 123 (2001) 362–369.
- [11] N. J. Driessen, C. V. Bouten, F. P. Baaijens, A structural constitutive model for collagenous cardiovascular tissues incorporating the angular fiber distribution (2005).
- [12] M. G. Geers, V. G. Kouznetsova, W. Brekelmans, Multi-scale computational homogenization: Trends and challenges, *Journal of computational and applied mathematics* 234 (2010) 2175–2182.
- [13] J. Fish, R. Fan, Mathematical homogenization of nonperiodic heterogeneous media subjected to large deformation transient loading, *International Journal for numerical methods in engineering* 76 (2008) 1044–1064.
- [14] A. N. Natali, E. L. Carniel, P. G. Pavan, P. Dario, I. Izzo, Hyperelastic models for the analysis of soft tissue mechanics: definition of constitutive parameters, in: *The First IEEE/RAS-EMBS International Conference on Biomedical Robotics and Biomechatronics*, 2006. BioRob 2006., IEEE, pp. 188–191.
- [15] A. D. Freed, D. R. Einstein, M. S. Sacks, Hypoelastic soft tissues, *Acta mechanica* 213 (2010) 205–222.
- [16] M. Alber, A. B. Tepole, W. R. Cannon, S. De, S. Dura-Bernal, K. Garikipati, G. Karniadakis, W. W. Lytton, P. Perdikaris, L. Petzold, et al., Integrating machine learning and multiscale modeling—perspectives, challenges, and opportunities in the biological, biomedical, and behavioral sciences, *NPJ digital medicine* 2 (2019) 1–11.
- [17] D. Reimann, K. Chandra, N. Vajragupta, T. Glasmachers, P. Junker, A. Hartmaier, et al., Modeling macroscopic material behavior with machine learning algorithms trained by micromechanical simulations, *Frontiers in Materials* 6 (2019) 181.
- [18] S. Bhattacharjee, K. Matouš, A nonlinear manifold-based reduced order model for multiscale analysis of heterogeneous hyperelastic materials, *Journal of Computational Physics* 313 (2016) 635–653.
- [19] P. Kerfriden, O. Gourg, T. Rabczuk, S. P.-A. Bordas, A partitioned model order reduction approach to rationalise computational expenses in nonlinear fracture mechanics, *Computer methods in applied mechanics and engineering* 256 (2013) 169–188.
- [20] Z. Liu, J. A. Moore, S. M. Aldousari, H. S. Hedia, S. A. Asiri, W. K. Liu, A statistical descriptor based volume-integral micromechanics model of heterogeneous material with arbitrary inclusion shape, *Computational Mechanics* 55 (2015) 963–981.
- [21] J.-C. Michel, P. Suquet, A model-reduction approach in micromechanics of materials preserving the variational structure of constitutive relations, *Journal of the Mechanics and Physics of Solids* 90 (2016) 254–285.
- [22] J. Oliver, M. Caicedo, A. E. Huespe, J. Hernández, E. Roubin, Reduced order modeling strategies for computational multiscale fracture, *Computer Methods in Applied Mechanics and Engineering* 313 (2017) 560–595.
- [23] B. Le, J. Yvonnet, Q.-C. He, Computational homogenization of nonlinear elastic materials using neural networks, *International Journal for Numerical Methods in Engineering* 104 (2015) 1061–1084.
- [24] K. Wang, W. Sun, A multiscale multi-permeability poroplasticity model linked by recursive homogenizations and deep learning, *Computer Methods in Applied Mechanics and Engineering* 334 (2018) 337–380.
- [25] C. Yang, Y. Kim, S. Ryu, G. X. Gu, Prediction of composite microstructure stress-strain curves using convolutional neural networks, *Materials & Design* 189 (2020) 108509.
- [26] G. C. Peng, M. Alber, A. B. Tepole, W. R. Cannon, S. De, S. Dura-Bernal, K. Garikipati, G. Karniadakis, W. W. Lytton, P. Perdikaris, et al., Multiscale modeling meets machine learning: What can we learn?, *Archives of Computational Methods in Engineering* (2020) 1–21.
- [27] A. B. Tepole, D. Nordsletten, K. Garikipati, E. Kuhl, Special issue on uncertainty quantification, machine learning, and data-driven modeling of biological systems, *CMAE* 362 (2020) 112832.
- [28] D. S. Clague, R. J. Phillips, A numerical calculation of the hydraulic permeability of three-dimensional disordered fibrous media, *Physics of Fluids* 9 (1997) 1562–1572.
- [29] V. K. Lai, S. P. Lake, C. R. Frey, R. T. Tranquillo, V. H. Barocas, Mechanical behavior of collagen-fibrin co-gels reflects transition from series to parallel interactions with increasing collagen content, *Journal of biomechanical engineering* 134 (2012).
- [30] L. A. Mihai, A. Goriely, Finite deformation effects in cellular structures with hyperelastic cell walls, *International Journal of Solids and Structures* 53 (2015) 107–128.
- [31] L. A. Mihai, H. Wyatt, A. Goriely, A microstructure-based hyperelastic model for open-cell solids, *SIAM Journal on Applied Mathematics* 77 (2017) 1397–1416.
- [32] M. Seeger, Gaussian processes for machine learning, *International journal of neural systems* 14 (2004) 69–106.
- [33] B. Schölkopf, K. Tsuda, J.-P. Vert, *Kernel methods in computational biology*, MIT press, 2004.
- [34] S. Group, et al., *Sheffieldml/gpy: Gaussian processes framework in python*, 2012.
- [35] A. L. Frankel, R. E. Jones, L. P. Swiler, Tensor basis gaussian process models of hyperelastic materials, *Journal of Machine Learning for Modeling and Computing* 1 (2020).
- [36] P. Virtanen, R. Gommers, T. E. Oliphant, M. Haberland, T. Reddy, D. Cournapeau, E. Burovski, P. Peterson, W. Weckesser, J. Bright, et al., *Scipy 1.0: fundamental algorithms for scientific computing in python*, *Nature methods* 17 (2020) 261–272.
- [37] G. Chagnon, M. Rebouah, D. Favier, Hyperelastic energy densities for soft biological tissues: a review, *Journal of Elasticity* 120 (2015) 129–160.
- [38] V. Avrutskiy, Backpropagation generalized for output derivatives, *arXiv preprint arXiv:1712.04185* (2017).
- [39] J. E. Prussing, The principal minor test for semidefinite matrices, *Journal of Guidance, Control, and Dynamics* 9 (1986) 121–122.
- [40] A. Botchkarev, Performance metrics (error measures) in machine learning regression, forecasting and prognostics: Properties and typology, *arXiv preprint arXiv:1809.03006* (2018).
- [41] B. L. Bowerman, R. T. O’Connell, A. B. Koehler, Forecasting, time series, and regression: an applied approach [cd] (2005).
- [42] D. P. Kingma, J. Ba, Adam: A method for stochastic optimization, *arXiv preprint arXiv:1412.6980* (2014).
- [43] D. E. Rumelhart, G. E. Hinton, R. J. Williams, Learning representations by back-propagating errors, *nature* 323 (1986) 533–536.

- [44] V. Nair, G. E. Hinton, Rectified linear units improve restricted boltzmann machines, in: ICML.
- [45] F. Chollet, et al., Keras: The python deep learning library, ascl (2018) ascl-1806.
- [46] M. Abadi, A. Agarwal, P. Barham, E. Brevdo, Z. Chen, C. Citro, G. S. Corrado, A. Davis, J. Dean, M. Devin, et al., Tensorflow: Large-scale machine learning on heterogeneous distributed systems, arXiv preprint arXiv:1603.04467 (2016).
- [47] N. S. Keskar, D. Mudigere, J. Nocedal, M. Smelyanskiy, P. T. P. Tang, On large-batch training for deep learning: Generalization gap and sharp minima, arXiv preprint arXiv:1609.04836 (2016).
- [48] A. G. Holzapfel, Nonlinear solid mechanics II, John Wiley & Sons, Inc., 2000.
- [49] S. Lin, L. Gu, Influence of crosslink density and stiffness on mechanical properties of type i collagen gel, *Materials* 8 (2015) 551–560.
- [50] V. Mullachery, A. Khera, A. Husain, Bayesian neural networks, arXiv preprint arXiv:1801.07710 (2018).
- [51] R. M. Neal, Bayesian learning for neural networks, volume 118, Springer Science & Business Media, 2012.
- [52] A. J. Licup, S. Münster, A. Sharma, M. Sheinman, L. M. Jawerth, B. Fabry, D. A. Weitz, F. C. MacKintosh, Stress controls the mechanics of collagen networks, *Proceedings of the National Academy of Sciences* 112 (2015) 9573–9578.
- [53] L. Zhang, Microstructural modeling of cross-linked fiber network embedded in continuous matrix, Rensselaer Polytechnic Institute, 2013.
- [54] M. Aghvami, K. L. Billiar, E. A. Sander, Fiber network models predict enhanced cell mechanosensing on fibrous gels, *Journal of biomechanical engineering* 138 (2016).
- [55] R. Raghupathy, V. H. Barocas, A closed-form structural model of planar fibrous tissue mechanics, *Journal of biomechanics* 42 (2009) 1424–1428.
- [56] M. Liu, L. Liang, W. Sun, A generic physics-informed neural network-based constitutive model for soft biological tissues, *Computer Methods in Applied Mechanics and Engineering* 372 (2020) 113402.